

Research Article

Open Access



# Molecular dynamics simulations of nanoparticle sintering in additive nanomanufacturing: insights from sintering mechanisms

Dourna Jamshideasli<sup>1,2</sup>, Nima Shamsaei<sup>1,2</sup>, Masoud Mahjouri-Samani<sup>1,3</sup>, Shuai Shao<sup>1,2</sup>

<sup>1</sup>National Center for Additive Manufacturing Excellence (NCAME), Auburn University, Auburn, AL 36849, USA.

<sup>2</sup>Department of Mechanical Engineering, Auburn University, Auburn, AL 36849, USA.

<sup>3</sup>Department of Electrical and Computer Engineering, Auburn University, Auburn, AL 36849, USA.

**Correspondence to:** Dr. Shuai Shao, Department of Mechanical Engineering, Auburn University, 354 War Eagle Way, Auburn, AL 36849, USA. E-mail: sshao@auburn.edu

**How to cite this article:** Jamshideasli D, Shamsaei N, Mahjouri-Samani M, Shao S. Molecular dynamics simulations of nanoparticle sintering in additive nanomanufacturing: insights from sintering mechanisms. *Green Manuf Open* 2024;2:16. <https://dx.doi.org/10.20517/gmo.2024.062001>

**Received:** 20 Jun 2024 **First Decision:** 13 Aug 2024 **Revised:** 12 Sep 2024 **Accepted:** 20 Sep 2024 **Published:** 8 Oct 2024

**Academic Editor:** Zhichao Liu **Copy Editor:** Pei-Yun Wang **Production Editor:** Pei-Yun Wang

## Abstract

The sintering behavior of nanoparticles (NPs), which determines the quality of additively nanomanufactured products, differs from conventional understanding established for microparticles. As NPs have a high surface-to-volume ratio, they are subjected to a higher influence from surface tension and a lower melting point than microparticles, resulting in variations in both crystallographic defect-mediated and surface diffusion mechanisms. Meanwhile, the interplay between these controlling mechanisms in NPs has not been well understood, primarily because sintering occurs on the nanosecond timescale, making it an exceptionally transient process. In this work, sintering of both equal and unequal sized Ag and Cu NP doublets with and without misorientation (both tilt and twist) is modeled through molecular dynamics (MD) simulations. The formation and evolution of crystallographic defects, such as vacancies, dislocations, stacking faults, twin boundaries, and grain boundaries, during sintering are investigated. The influence of these defects on plastic deformation and diffusion mechanisms, such as volume diffusion and grain boundary (GB) diffusion, is discussed to elucidate the responsible sintering mechanisms. The surface diffusion mechanism is visualized by using detailed atomic trajectories generated during the sintering process. Finally, the overall effectiveness of all diffusion sintering mechanisms is quantified. This study provides first insights into the complexity and dynamics of NP sintering mechanisms which can aid in the development of accurate predictive models.

**Keywords:** Additive nanomanufacturing, sintering, nanoparticles, molecular dynamics, mechanisms, crystallographic defects



© The Author(s) 2024. **Open Access** This article is licensed under a Creative Commons Attribution 4.0 International License (<https://creativecommons.org/licenses/by/4.0/>), which permits unrestricted use, sharing, adaptation, distribution and reproduction in any medium or format, for any purpose, even commercially, as long as you give appropriate credit to the original author(s) and the source, provide a link to the Creative Commons license, and indicate if changes were made.



## INTRODUCTION

Laser-based additive nanomanufacturing (ANM) technique offers a sustainable path for creating real-life applications such as wearable electronics and sensors. This promise stems from its two unique capabilities. First, ANM utilizes on-demand nanoparticle (NP) generation, eliminating the need for hazardous inks and solvents which translates to a safer and cleaner manufacturing process. Second, this procedure leverages biodegradable substrates which decompose naturally at the end of their lifespan contributing to a more sustainable product<sup>[1-7]</sup>. However, a critical step in ANM, sintering the deposited NPs, presents a challenge. Fine-tuning the laser parameters (time and energy) to achieve the desired sintered state can be challenging. Predictive models can offer a solution by describing the sintering process, minimizing material waste and energy consumption during optimization.

Two main approaches to describing sintering are data-driven and mechanism-oriented models<sup>[8]</sup>. The data-driven models use quantitative data to predict sintering, whereas the mechanism-oriented models involve physical theories based on mechanism knowledge to elucidate and potentially predict sintering. Numerous data-driven models quantify the parametric effects of various NP characteristics, such as NP size and sintering conditions (e.g., temperature), on sintering outcomes without necessarily delving into all the underlying mechanisms<sup>[9-12]</sup>. However, understanding of the governing mechanisms for these effects, and how these mechanisms transition from one to another as NP sintering proceeds, is still largely lacking and such knowledge is beneficial for refining predictive sintering models.

This work aims to shed light on the governing sintering mechanisms by examining different defects and visualizing atomic diffusion paths in sintered NPs. To achieve this, the study uses molecular dynamics (MD) simulations to visualize four key mechanisms, including three diffusion-based mechanisms [i.e., lattice diffusion, surface diffusion, and grain boundary (GB) diffusion] and one mechanism mediated by plastic deformation. The simulations are performed on NPs of equal size, unequal size, and with tilted and twisted misorientation angles, under different sintering temperatures. Moreover, the trajectories of atoms involved in neck formation, from each NP to the neck region, are determined.

This article is organized as follows: Section “LITERATURE REVIEW” reviews the current understanding of sintering mechanisms, highlighting both established knowledge and significant gaps. Section “METHODOLOGY” explains the simulation methodology. Section “RESULTS AND DISCUSSION” discusses simulation results, including the distributions of different defects over time (Section “Analysis of defects to assess crystallographic defect-mediated sintering mechanisms”) and the overall effectiveness of all diffusion sintering mechanisms through atomic trajectories and analyses of surface diffusion (Section “Collective contribution of diffusion-based mechanisms to sintering”). Some future directions and broader research opportunities are discussed in “PERSPECTIVE AND OUTLOOK”. Finally, the conclusions are drawn in Section “CONCLUSION”.

## LITERATURE REVIEW

Conventional treatments of sintering mechanisms categorize them by the different paths that material flows in response to the sintering driving force<sup>[13-16]</sup>. The identified controlling sintering mechanisms contribute to sintering through diffusion, plastic flow, and vapor transport<sup>[17,18]</sup>. **Figure 1** shows a pair of sintered particles with several arrows (1-6) indicating distinct material flow paths originating from both the exterior surfaces and interior volumes of particles. These arrows also depict the accumulation of material in the neck region. To account for the many sintering mechanisms, mathematical relations have been introduced to predict the

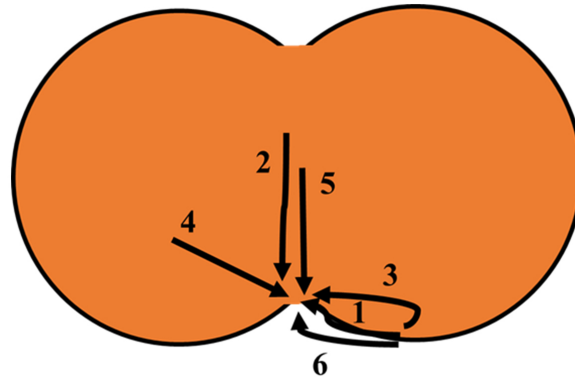


**Figure 1.** A schematic of different material transport paths influencing sintering. Arrows represent the movement of atoms during each mechanism. The sintering mechanisms categorized by arrows are (1) surface diffusion, (2 and 3) lattice diffusion, (4) plastic flow, (5) GB diffusion, and (6) vapor transport. GB: Grain boundary.

rate of microparticle sintering<sup>[17]</sup>.

In conjunction with conventional treatments, MD simulations have emerged as a powerful tool for investigating NP sintering. MD simulations excel at capturing the short time and small length scales crucial to understanding the NP sintering process. However, these studies typically oversimplify the mechanisms by leaving out the combined effects of various mechanisms that are active at different stages and contribute differently to the overall sintering process<sup>[19-25]</sup>. For instance, in most MD studies, several of the six aforementioned mechanisms [Figure 1] have been identified as critical in the neck size growth, with a particular emphasis on the occurrence of surface diffusion, lattice diffusion, and GB diffusion (not always including all three)<sup>[26-29]</sup>. Moreover, several studies have estimated surface and GB diffusion coefficients by assuming these two mechanisms are the only ones active throughout the sintering process<sup>[26,28]</sup>.

Crystallographic defects, such as vacancies, stacking faults, twin boundaries, and GBs, may appear during the sintering of NPs. These defects play a crucial role in diffusion. For instance, atoms with sufficient energy and close to empty sites in lattice structures (i.e., vacancies) can hop from their original positions into these empty sites due to their thermal vibration<sup>[30]</sup>. Since lattice mass diffusion occurs via the motion of vacancies, analyzing the vacancy dynamics is important for understanding the role of lattice diffusion during sintering. Lattice diffusion activity is positively correlated with the number of vacancies present. Moreover, dislocations and GBs provide alternative diffusion pathways<sup>[31-33]</sup>. Furthermore, the interplay between defects, such as vacancies and GBs<sup>[22]</sup> or dislocations, when they coexist, may affect the population and spatial arrangements of these defects<sup>[34]</sup>. Even though previous MD studies<sup>[19-23]</sup> have provided valuable insight into defect structures, a comprehensive mechanistic understanding of how these defects influence sintering for different NP characteristics and sintering conditions is still lacking.

## METHODOLOGY

The MD simulations of the sintering process of a pair of NPs included four stages. A microcanonical ensemble (NVE) was implemented in Stage 1 for 5 ps and an equilibrium structure for each NP was achieved at the end of Stage 1. Subsequently, a canonical ensemble (NVT) was applied through Stage 2 for 5 ps to regulate the NP's temperature to room temperature (300 K). Each NP was then heated to a sintering temperature through an NVT ensemble within a constant heating time (~30 ps) in Stage 3. At the inception of sintering in Stage 4, two NPs were brought together to form a neck and an NVT ensemble was used to keep the two NPs at the selected sintering temperature for 5,000 ps. It is worth noting that the rate of

temperature increase in Stage 3 can influence the formation of initial necks and sintering mechanisms, particularly when both NPs are nearby and being heated simultaneously to a target temperature. However, the MD approach in this study was specifically designed to minimize such effects. Each NP was heated individually before being brought together, and sintering was conducted over an extended period during a subsequent isothermal stage. Moreover, the absence of a temperature gradient between the NPs as each was brought to the desired temperature through the same stages, further minimizing any possible influence of a different heating rate.

Ag and Cu NPs, nominally spherical in shape and possessing face-centered cubic (FCC) lattice structures, were modeled in side-by-side arrangements. Their crystallographic directions were chosen along the Cartesian axes according to the specific category (i.e., NPs of equal size, unequal size, and with tilted or twisted misorientation angles) being investigated. For instance, for NPs of both equal and unequal sizes without tilt or twist, the crystallographic orientations  $[1\ 0\ 0]$ ,  $[0\ 1\ 0]$ , and  $[0\ 0\ 1]$  were aligned with the X-, Y-, and Z-axes, respectively<sup>[35]</sup>. The initial distance between the surfaces of two spherical NPs refers to the gap between the outmost atoms of the two NPs along the line connecting the NPs' centroids. This distance was set as the equilibrium interatomic distance of the corresponding bulk material. Existing literature data on lattice parameters at various temperatures, in conjunction with the material's linear thermal expansion coefficient, was used to extrapolate and estimate the equilibrium lattice parameter at the desired temperature<sup>[36,37]</sup>. This was done to avoid excessive initial attractive and repulsive forces.

The embedded atom method (EAM) was used to model interatomic forces between Ag atoms<sup>[38]</sup> in Ag NPs and Cu atoms<sup>[39]</sup> in Cu NPs. Each direction in the simulation box was subjected to a shrink-wrapped boundary condition. The time step for simulations was set to 5 fs, which was sufficiently small to accurately capture the dynamics of the system under investigation<sup>[40-42]</sup>. This study involved systematically parameterizing NP size, size ratio, sintering temperature, misorientation angles, and material, which corresponded to 78 individual simulation cases. Five distinct NP diameters were modeled: 5, 10, 15, 20, and 25 nm. These diameters were chosen based on scanning electron microscope images, which showed that the size of the NPs generated and sintered using an *in-situ* laser-based ANM technique typically fell within this range<sup>[43]</sup>. To maintain solid-state sintering below their respective melting points<sup>[16,29]</sup>, the sintering temperatures were set at 50%, 60%, and 70% of the bulk melting points ( $T_m$ ) of Ag (1,234.95 K)<sup>[44]</sup> and Cu (1,358.15 K)<sup>[45]</sup>. A temperature of 70% of  $T_m$  was selected, instead of any higher temperatures, to compensate for lower melting temperatures typically exhibited by NPs. There were two symmetric tilted misorientation angles about the tilt axis of  $[1\ 0\ 0]$  studied, i.e.,  $36.87^\circ$  and  $53.15^\circ$ , which resulted in the formation of stable GBs with low energy states<sup>[46,47]</sup>. As twist GBs are not stable, the same angles were used for NPs with twisted misorientation angles about the twist axis of  $[0\ 0\ 1]$ . Each simulation case was designated with a set of parameters as Material\_Diameters\_Temperature\_Tilt-Twist to facilitate easy differentiation and reference. More details about the studied examples and simulation procedure can be found in an early work by the authors<sup>[12]</sup>.

MD simulations of each pair of NPs under different sintering conditions were conducted using the open-source large-scale atomic/molecular massively parallel simulator (LAMMPS)<sup>[48]</sup>. Moreover, the open visualization tool (OVITO)<sup>[49]</sup> was used to visualize and interpret the results. For visualization purposes only, a "quench" technique based on the Polak-Ribiere conjugate gradient algorithm<sup>[50]</sup> was applied at specific time steps to remove thermal fluctuations caused by random motions and distinguish atoms in various local lattice structures. Exemplar visualizations of crystallographic defects such as vacancies, stacking faults, and GBs are marked with light blue, black, and green arrows, respectively, in Figure 2. A polyhedral template matching method<sup>[51]</sup> was used to study local lattice structures. For a better view of

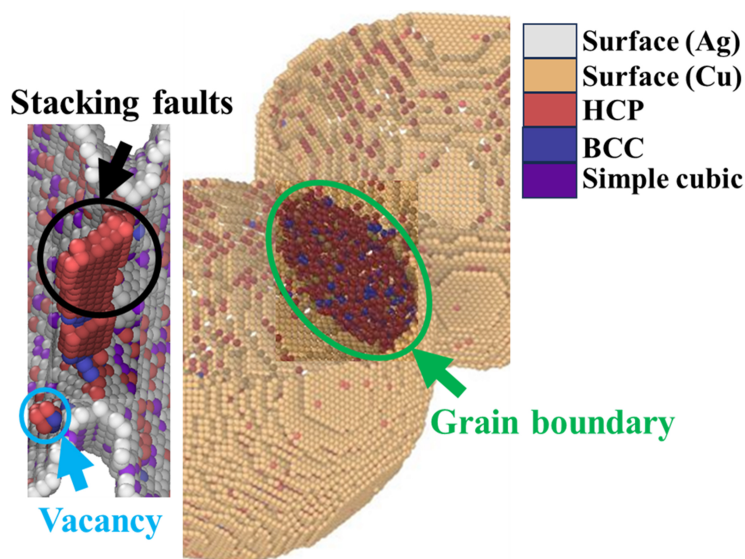


**Figure 2.** Exemplar visualizations of a vacancy, an intrinsic stacking fault, and a GB. GB: Grain boundary.

defects, the atoms forming FCC structures were removed. Red and blue colors in the atomistic snapshot corresponded to the locally hexagonal closed-packed (HCP) and body-centered cubic (BCC) lattice structures, respectively. The gray and orange colors corresponded to the surface atoms of Ag NPs and Cu NPs, respectively. A vacancy is the absence of an atom from its regular crystallographic lattice site. Vacancies and other defects disrupt the orderly atomic arrangements (periodicity). In visualized atomic structures, where the perfect FCC atoms were removed, vacancies typically appeared as being surrounded by aggregates of atoms. Twin boundaries and stacking faults were visible as a single layer of atoms and two or more adjacent atomic layers, respectively<sup>[49]</sup>. Furthermore, Shockley partials were connected by stacking faults. GBs were apparent in NPs with tilted and twisted misorientations. A GB typically appeared as a circular, planar layer of atoms in the neck region. Given the higher surface-to-volume ratio in NPs compared to bulk materials, these defects (vacancy, stacking fault, GB) are expected to have a significant impact on the properties and behavior of sintered NPs<sup>[52]</sup>.

Although MD simulations are effective in revealing detailed sintering mechanisms, their inherent limitations are also worthwhile to note. For instance, simulating realistic sintering processes involving a powder bed with a distribution of NPs becomes computationally expensive when attempting to model large systems or the long timescales necessary to reach the final sintering stage. Additionally, the accuracy of MD simulations relies on that of interatomic potential potentials. Due to these limitations, careful consideration for the MD simulations needs to be made to ensure that they target specific sintering phenomena and the interatomic potentials selected can capture such phenomena well.

## RESULTS AND DISCUSSION

This section presents the analysis of the MD simulation results regarding the sintering mechanisms at play for different NP characteristics and sintering temperatures. Section “Analysis of defects to assess crystallographic defect-mediated sintering mechanisms” includes crystallographic defect-mediated sintering mechanisms in NPs of similar and varying sizes, as well as those exhibiting misorientation angles including both tilt and twist. Subsequently, Section “Collective contribution of diffusion-based mechanisms to sintering” shifts focus to describe the collective action of all diffusion-based sintering mechanisms. Atomic paths are visualized to elucidate diffusion. Moreover, visualization of atomic paths provides a

complementary mechanistic understanding of surface diffusion. The total diffusion coefficients ( $D_{tot}$ ) are also calculated to compare the collective effectiveness of all diffusion-based mechanisms among cases.

### Analysis of defects to assess crystallographic defect-mediated sintering mechanisms

The distribution of defects, including vacancies, dislocations, stacking faults, and twin boundaries, inside equal-sized NPs is shown in Figure 3A-D. Lattice diffusion is evidenced by the observation of vacancy concentrations and their movement across different time frames, with snapshots illustrating this behavior at various stages of the simulation. These vacancy movements confirm the occurrence of lattice diffusion<sup>[53]</sup>. In the selected examples, defects were visualized at the beginning and final stages of sintering at 1,000 and 5,000 ps, respectively. The beginning and final stages of simulated sintering are shown in the left and right columns in Figure 3A-D, respectively. Compared to Cu NPs, sintered Ag NPs contained more stacking faults and twin boundaries, which indicated more severe plastic deformation (e.g., see Final at the bottom of Figure 3A and Final at the bottom of Figure 3B)<sup>[54]</sup>. In some examples, there were no defects at the end of the simulation (e.g., see Final at the top of Figure 3B and Final at the bottom of Figure 3C). In these cases,

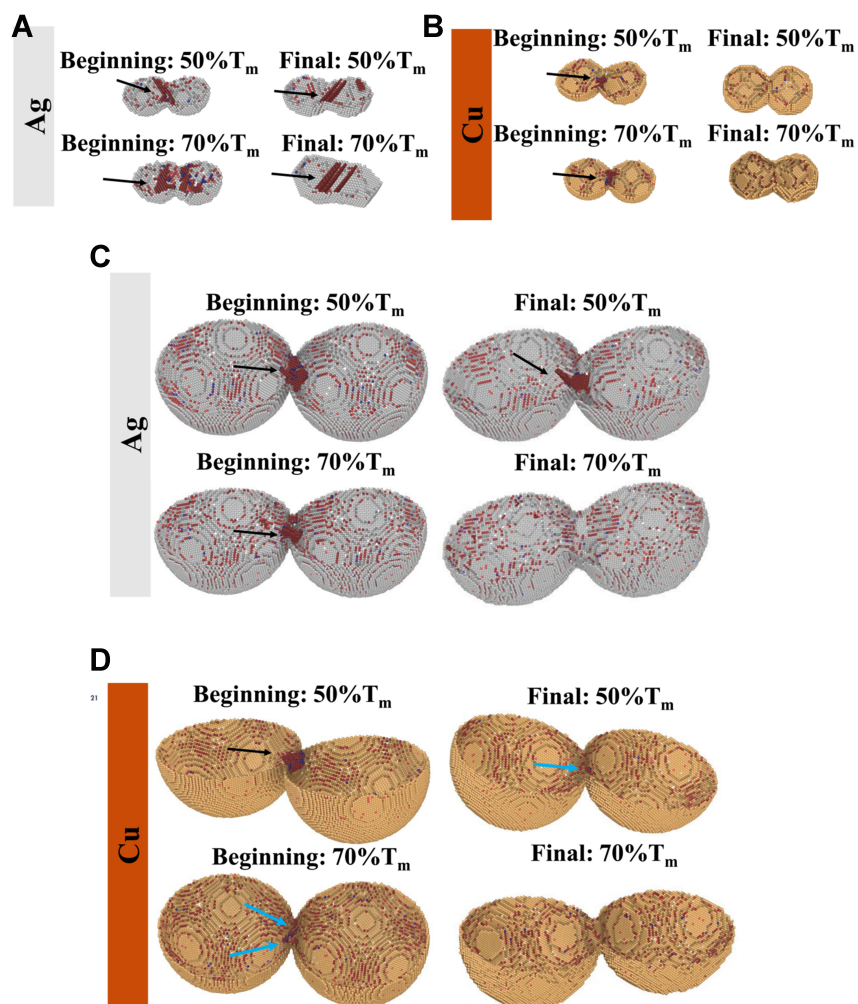


**Figure 3.** Distributions of vacancies, dislocations, stacking faults, and twin boundaries at both the beginning and final stages of sintering simulations for equal-sized NPs of (A) 5 nm Ag NPs, (B) 5 nm Cu NPs, (C) 15 nm Ag NPs, and (D) 15 nm Cu NPs. Two studied sintering temperatures are 50% $T_m$  and 70% $T_m$ . Black arrows mark dislocations, stacking faults, and twin boundaries, while light blue arrows point to vacancies. See [Supplementary Materials](#) for animations of selected key events. NPs: Nanoparticles;  $T_m$ : bulk melting points.

only surface diffusion was suspected to be the governing sintering mechanism at least for a short period leading to the final simulation time step.

Since the vacancies were only checked at certain times, their absence did not imply that they were never present. There were several examples in which vacancies existed at the end of the simulation, indicating that lattice diffusion was present even close to the final stage of sintering (see Final at the top of Figure 3D). Moreover, larger NPs were more likely to include vacancies than smaller ones, which could lead to increased lattice diffusion by providing additional jump sites for atoms. This was probably because vacancies had longer paths to move to the surface of the NPs in larger NPs and they had a higher chance of survival (compare Final at the top of Figure 3B vs. Final at the top of Figure 3D). Stacking faults might also remain at/near the neck region until the end of the simulation (see Final at the top of Figure 3C). Furthermore, the density of dislocations, stacking faults, and twin boundaries was higher in smaller NPs relative to their size. This was possibly due to smaller NPs having a higher surface area to volume ratio, which increased the driving force for defect formation to minimize total surface energy per unit volume through strain relaxation (compare Final at the top of Figure 3A vs. Final at the top of Figure 3C). Although the travel distance of defects in larger NPs might be comparable to those in smaller NPs, the defects' movements were restricted to a proportionally smaller region within the larger NP, particularly concentrated near the neck regions. In smaller NPs, the defects could reach close to the interior volume of NPs, probably due to the short distance between the neck and surface (compare the top of Figure 3A vs. the top of Figure 3C).

Several additional instances of equal-sized NPs that provide additional insights are shown in Figure 4A-G.

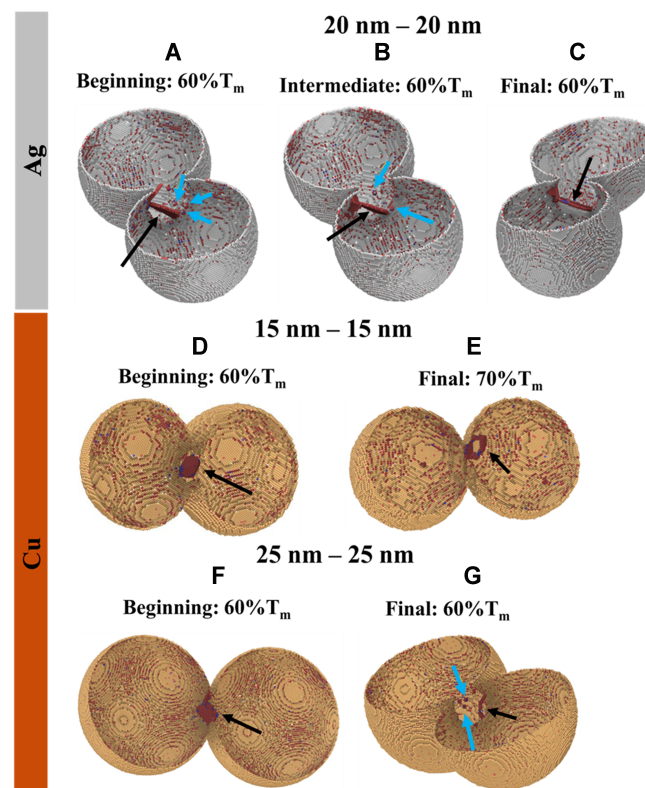


**Figure 4.** Distributions of vacancies, dislocations, stacking faults, and twin boundaries in equal-sized NPs for (A-C) 20 nm Ag NPs sintered at  $60\%T_m$  at the beginning, intermediate, and final stages of sintering; (D and E) 15 nm Cu NPs sintered at  $60\%T_m$  and  $70\%T_m$  at the final stage; (F and G) 25 nm Cu NPs sintered at  $60\%T_m$  at the beginning and final stages of sintering. Black arrows mark dislocations, stacking faults, and twin boundaries, while light blue arrows point to vacancies. See [Supplementary Materials](#) for animations of selected key events. NPs: Nanoparticles;  $T_m$ : bulk melting points.

In the context of the figures, the intermediate stage of sintering refers to a time step between 1,000 and 5,000 ps. Ag NPs displayed stacking faults and dislocations with dimensions comparable to their necks [Figure 4C]. As dislocations glide, they can potentially interact with other defects such as other dislocations and vacancies<sup>[34,55,56]</sup>. The interplay between these interactions can significantly impact diffusion behavior during sintering. In the specific example of Ag<sub>20-20\_60%</sub> $T_m$ -0-0 [Figure 4A-C], a vacancy moved next to a dislocation and disappeared (likely due to being absorbed by the dislocation). However, this absorption did not eliminate the vacancy. Instead, the vacancy became incorporated within the core of the dislocation. During simulated sintering time, several examples exhibited stacking faults [Figure 4D] or dislocation loops [Figure 4E] in the neck region. These stacking faults likely signaled the initial stage of dislocation nucleation. Line tension typically shrinks the dislocation loop until they disappear. However, defects can pin these loops, hindering their annihilation<sup>[57]</sup>. The persistence of loops in the simulation suggested pinning by defects, likely jogs in this case. For Cu<sub>25-25\_60%</sub> $T_m$ -0-0 [Figure 4F], initially longer partial dislocations possibly interacted with other dislocations. This interaction might have resulted in the formation of shorter, sessile dislocations and vacancy emission [Figure 4G]. These vacancies likely appeared due to jogs on the dislocations undergoing climb or spontaneous vacancy generation. Notably, these vacancies persisted throughout the simulation, including the final time step.

The distribution of defects, particularly vacancies, dislocations, stacking faults, and twin boundaries, inside unequal-sized NPs is shown in Figure 5A-D. As with sintering of similarly sized NPs, plastic deformation

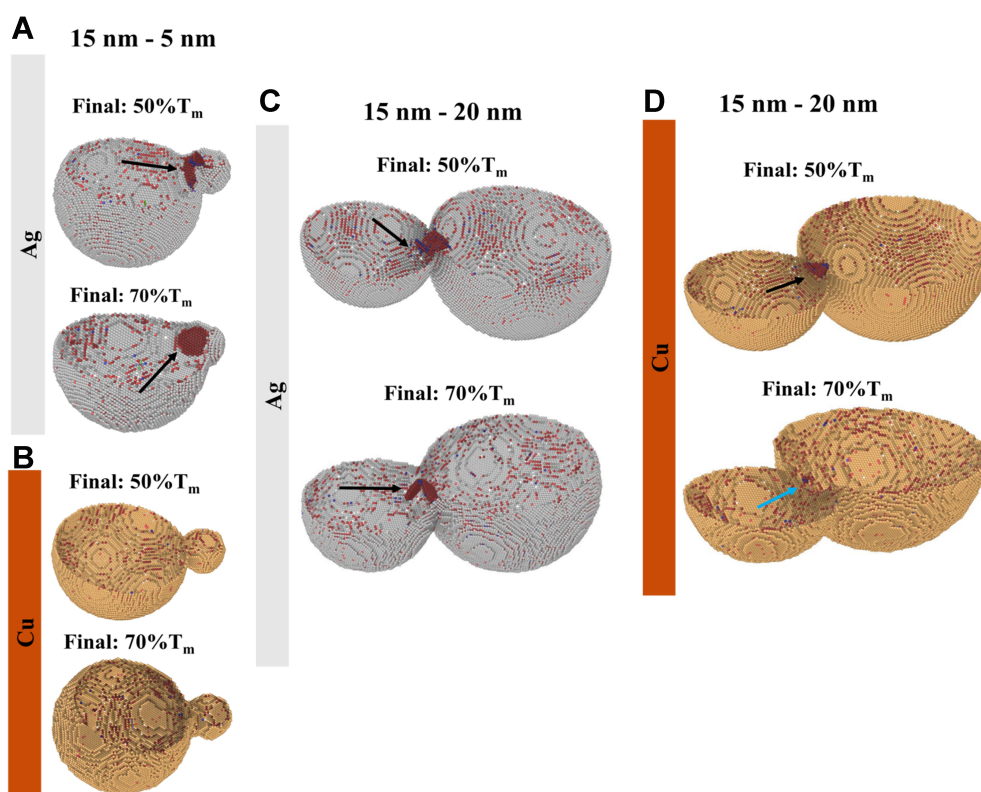


**Figure 5.** Distribution of vacancies, dislocations, stacking faults, and twin boundaries at the final sintering stage for unequal-sized NPs sintered at 50% $T_m$  and 70% $T_m$ . Size ratios: (A) Ag, 3:1; (B) Cu, 3:1; (C) Ag, 1.33:1; (D) Cu, 1.33:1. Black arrows mark dislocations, stacking faults, and twin boundaries, while light blue arrows point to vacancies. See [Supplementary Materials](#) for animations of selected key events. NPs: Nanoparticles;  $T_m$ : bulk melting points.

was more pronounced in Ag NPs than in Cu ones. Notably, several examples did not have any defects during a short period leading to the final simulation time step. In these cases, surface diffusion was suspected to contribute to neck growth (e.g., see bottom and top in [Figure 5B](#)). In the beginning of sintering for Cu<sub>15-20-70%T<sub>m-0-0</sub>, a higher concentration of vacancies was observed in the larger NP. However, as sintering progressed, these vacancies migrated towards the smaller NP, ultimately residing in the smaller NP at the final frame of simulation (e.g., see the top of [Figure 5D](#)). Considering Ag<sub>15-5-70%T<sub>m-0-0</sub>, dislocations were located within the larger NP at the beginning of simulation. However, these dislocations migrated towards the surface through the movements of kinks and jogs at the subsequent time steps. By the end of simulation, the dislocations were positioned very close to the surface (see the bottom of [Figure 5A](#)). This was probably due to expedited diffusion, particularly given the high temperature and large size ratio in Ag<sub>15-5-70%T<sub>m-0-0</sub><sup>[58]</sup>. In Ag NPs with a larger equivalent diameter, dislocations were more likely to multiply within the neck region. However, the impingement of these dislocations near the final stage of sintering was likely to suppress the nucleation of any new dislocations (e.g., compare bottom and top in [Figure 5C](#))<sup>[19]</sup>.</sub></sub></sub>

The distributions of defects, particularly GBs inside NPs with tilt and twist misorientations are depicted in [Figure 6A-D](#) and [Figure 7A-D](#), respectively. At an early stage of the sintering process, a GB persisted at the

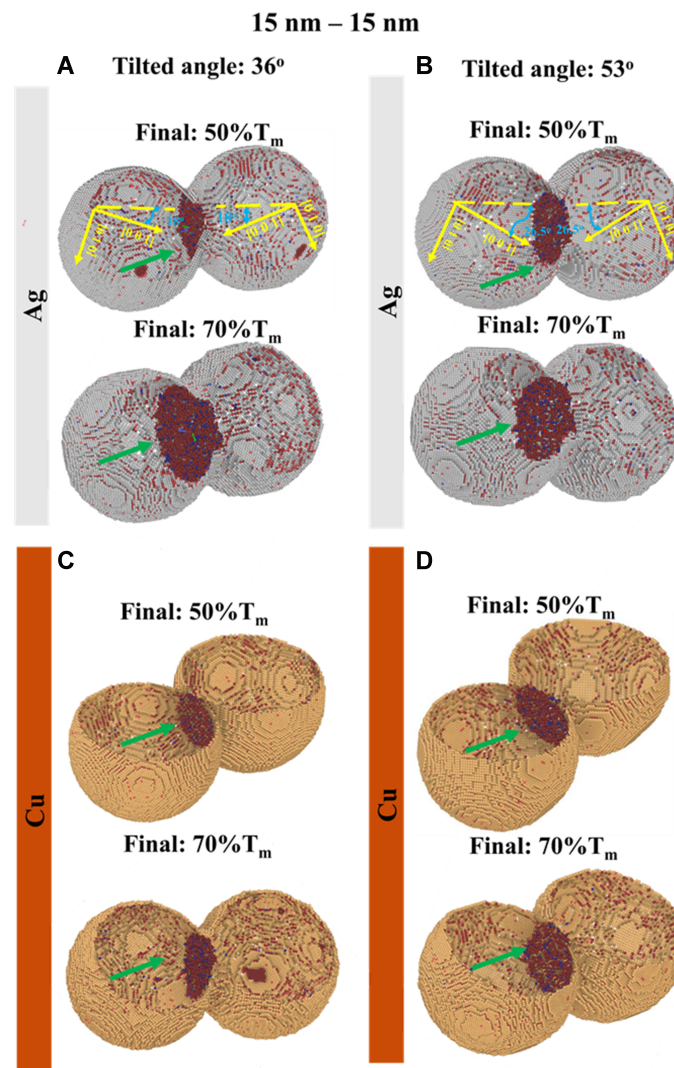


**Figure 6.** Distribution of GBs at the final sintering stage for 15 nm NPs with tilted misorientation angles of (A)  $36.87^\circ$ , (B)  $53.15^\circ$  for Ag NPs, and (C)  $36.87^\circ$ , (B)  $53.15^\circ$  for Cu NPs. Two sintering temperatures of  $50\%T_m$  and  $70\%T_m$  are included. The green arrows point to GBs. See [Supplementary Materials](#) for animations of selected key events. GBs: Grain boundaries; NPs: nanoparticles;  $T_m$ : bulk melting points.

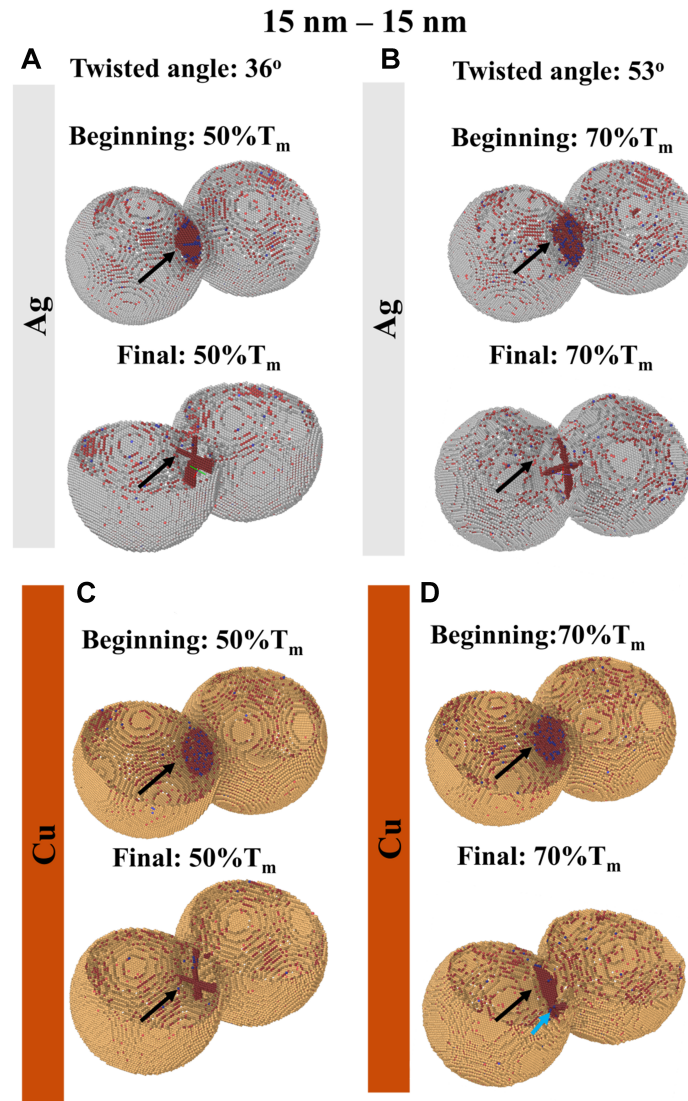


**Figure 7.** Distribution of vacancies, GBs, and dislocations at the beginning and final sintering stages for 15 nm NPs with twisted misorientation angles of (A)  $36.87^\circ$ , (B)  $53.15^\circ$  for Ag NPs, and (C)  $36.87^\circ$ , (B)  $53.15^\circ$  for Cu NPs. Two sintering temperatures of  $50\%T_m$  and  $70\%T_m$  are included. Green arrows point to GBs. Black arrows highlight GBs with wider spacings between screw dislocations. Light blue arrows point to vacancies. See [Supplementary Materials](#) for animations of selected key events. GBs: Grain boundaries; NPs: nanoparticles;  $T_m$ : bulk melting points.

neck between NPs with tilted misorientation angles. This suggested that diffusion through GBs was possibly active throughout the sintering process. Moreover, at higher temperatures and a misorientation angle of  $36.85^\circ$ , the GB was more pronounced, and the neck region was wider, indicating a more effective GB

diffusion mechanism (e.g., compare bottom of [Figure 6A](#) and bottom of [Figure 6B](#)). Edge dislocations in GBs with tilt misorientation possess Burgers vector components perpendicular to the GB plane. Consequently, due to their non-planar glide motion, GB dislocations were unable to readily escape, preventing the formation of untitled NPs. Akin to NPs with tilted misorientation angles, those with twisted misorientation angles also developed a GB. However, in twist GBs, a network of screw dislocations with Burgers vectors parallel to the GB plane exists. These screw dislocations exert repulsive forces on each other, leading to an increase in their spacing within the GB. This can even result in some dislocations escaping the GB surface. Consequently, the overall dislocation density within the GB decreases, which, in turn, reduces the twist misorientation angle and ultimately leads to the untwisting of the NPs (e.g., see the bottom of [Figure 7C](#)). This behavior suggested that GB diffusion remained active only during the beginning of sintering for NPs with twisted misorientation angles.

### **Collective contribution of diffusion-based mechanisms to sintering**

This section explains how the previously visualized defects relate to atomic trajectories. To generate these atomic paths, the atoms that formed the neck were first identified. This was achieved by dissecting the region near the neck into thin slices, each with a thickness of 2 Å, perpendicular to the doublet's long axis. The neck region was detected based on the fewest atoms within a slice. Notably, all these atoms originated from the surfaces of the NPs. The trajectories of these neck atoms were shown at time intervals of 1,000 ps to depict their movements toward the neck region. Below the snapshots in [Figures 8-10](#), rainbow color bars display the trajectory color codes to distinguish different time intervals. For example, the pieces of trajectory lines in red and blue colors represent the time intervals from 0 to 1,000 ps and from 4,000 to 5,000 ps, respectively. In addition, the starting positions of the neck atoms are highlighted with slightly larger, dark grey spheres.

Drawing upon the categorization of sintering mechanisms based on the transport pathways in [Figure 1](#), surface diffusion was only considered active when the entire trajectory of an atom remained on the NP surface. Conversely, trajectories confined to the interior volume of NPs suggest diffusion processes such as GB diffusion, lattice diffusion, or pipe diffusion along dislocations. This excludes surface diffusion, which occurs at the NP's exterior. For NPs without misorientations, the trajectories passing through the NPs indicate either lattice or pipe diffusion. In regions with dislocations and without vacancies, pipe diffusion is prevalent until vacancies appear, at which point lattice diffusion may occur, facilitating sintering by adding atomic pathways. The transition between pipe and lattice diffusion, or their coexistence, can occur rapidly within just several picoseconds. In NPs with tilt misorientations, GB diffusion is evident from trajectories that align towards the GB, without following the surfaces of NPs. For NPs with twist misorientations, GB diffusion may initiate atomic movement, but as the GBs are transient, diffusion pathways often shift to pipe diffusion along dislocations.

The extent of neck growth is reflected by the number of neck atoms and their corresponding trajectories. Importantly, each atom reaching the neck does so through the action of one or a combination of the governing sintering mechanisms. In all the visualizations in this section, the trajectories of all the neck atoms are shown, implying that the contributions of all diffusion-based sintering mechanisms, including surface diffusion, are inherently accounted for. The analysis of the characteristics of these trajectories, such as their concentrations and lengths, can indicate the collective effectiveness of all governing sintering

mechanisms. The number of visualized atomic paths (trajectories) directly correlates with sintering effectiveness. This qualitative observation is further supported quantitatively by calculating the  $D_{tot}$ .  $D_{tot}$  is a measure of the total diffusive transport and, hence, the collective contribution of diffusion-based sintering mechanisms. To quantify  $D_{tot}$ , the mean square displacement (MSD) was calculated and then implemented in Einstein-Smoluchowski's diffusion formula<sup>[24]</sup>. MSD measures the cumulative effect of random atomic displacements over time by averaging the squared distance between their initial and final positions.

$$MSD = \frac{1}{N} \sum_{i=1}^N (r_i(t) - r_i(0))^2 \quad (1)$$

where  $N$  is the total number of atoms, and  $r_i(t)$  is the displacement of the  $i^{\text{th}}$  atom from its initial position  $r_i(0)$  during  $t$  time period. The slope of the MSD vs. time curve is directly proportional to the diffusion coefficient ( $D$ ), as predicted by Einstein-Smoluchowski's diffusion formula, i.e.,

$$D = \frac{1}{2f} \frac{dMSD}{dt} \quad (2)$$

where  $t$  is time, and  $f$  is the degree of freedom, and it equals 2 for surface diffusion or GB diffusion, and 3 for lattice diffusion. Diffusion coefficients are inversely proportional to the denominator  $f$  value. For a case involving concurrent surface, volume, and GB diffusion, the equation implies that surface and GB diffusions contribute more to sintering than bulk diffusion because they have lower  $f$  values. This study assumed that the slope of the MSD curve (i.e.,  $dMSD/dt$ ) represented the  $D_{tot}$ , encompassing all underlying mechanisms. It is worth noting that while gravity-induced plastic flow can significantly influence diffusion behavior under certain conditions, its effect on the ANM is negligible due to the miniscule size of NPs and the thin layers of electronics being fabricated. Accordingly, simulation conditions in this study included constant temperature, no external pressure, and shrink-wrapped boundary conditions. The calculated values of  $D_{tot}$  were added to the figures in this section for comparison purposes.

The trajectories of the atoms that built up the neck in equal-sized NPs are displayed in [Figure 8A-D](#). Higher temperatures facilitated the involvement of a greater number of atoms in the neck growth, which was evident from the increased number of trajectory lines and their extended lengths. This signified enhanced effectiveness of sintering mechanisms, as corroborated by higher  $D_{tot}$  values (e.g., compare the top and the bottom of [Figure 8A](#)). At a particular temperature, the shorter diffusion paths of atoms belonging to smaller NPs, relative to those in larger ones, increased the accessibility of atoms closer to the surrounding regions to reach the neck region (e.g., see the bottom of [Figure 8B](#) vs. the bottom of [Figure 8D](#)). Furthermore, at a given temperature, Ag NPs with identical diameters exhibited more diffusion pathways, and their atoms traveled farther than those of Cu NPs. This suggested that sintering mechanisms were more effective in Ag NPs, further supported by their higher  $D_{tot}$  values (e.g., see the bottom of [Figure 8C](#) vs. the bottom of [Figure 8D](#)).

The trajectories of atoms that built up the neck in unequal-sized NPs are displayed in [Figure 9A-D](#). As diffusion controlled both the sintering processes for NPs of equal and unequal sizes, the trajectories of NPs with differing sizes were subjected to a similar analysis. Across all cases, the greater number of atoms forming the neck regions at higher temperatures resulted in a larger number of trajectory lines and showed a correlation with larger  $D_{tot}$  values (e.g., compare the top of [Figure 9A](#) and the bottom of [Figure 9A](#)). Moreover, comparing Ag and Cu NPs, Ag displayed a greater number of longer-distance trajectories, indicating more effective sintering mechanisms, as corroborated by their higher  $D_{tot}$  values (e.g., compare the bottom of [Figure 9C](#) and the bottom of [Figure 9D](#)). However, the diffusion paths for NPs of varying sizes differed from uniformly sized NPs, exhibiting several key variations due to the presence of a

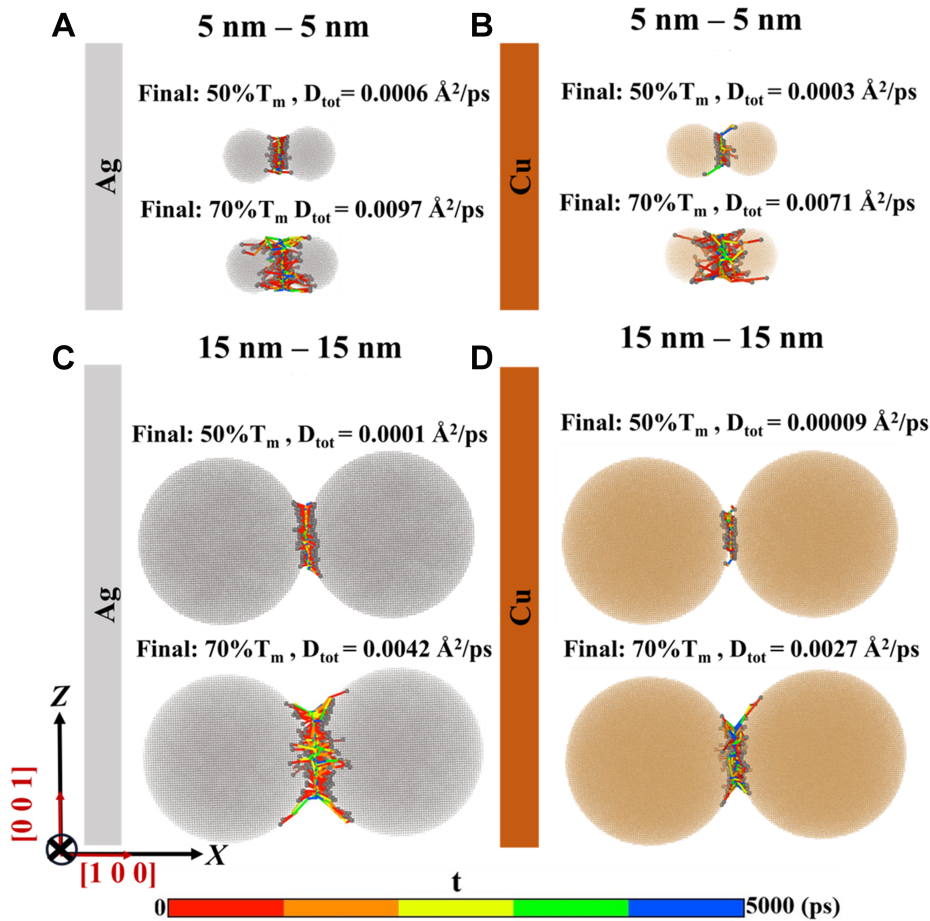


**Figure 8.** Examples of atomic trajectories of NPs with identical sizes at sintering temperatures of 50%  $T_m$  and 70%  $T_m$ : (A) 5 nm Ag NPs, (B) 5 nm Cu NPs, (C) 15 nm Ag NPs, and (D) 15 nm Cu NPs. See [Supplementary Materials](#) for animations of selected key events. NPs: Nanoparticles;  $T_m$ : bulk melting points.

differential pressure induced by surface tension between the two NPs. The greater number of trajectories from the smaller NP to the neck indicated that the atoms from the smaller NP contributed more substantially to the neck growth than the larger NP in the pair (see the bottom of [Figure 9A](#)). This observation suggested that the sintering mechanisms were more strongly influenced by the characteristics of the smaller NPs. This implication remained valid when the particle size ratio was closer to unity and the NPs involved were larger. Moreover, in NPs with a size ratio close to one, the contributions from atoms in larger NP to the neck region were more apparent (compare the bottom of [Figure 9A](#) and the bottom of [Figure 9C](#)).

The trajectories of atoms that built up the neck in NPs with tilted and twisted misorientation angles are displayed in [Figure 10A-H](#). The values of  $D_{tot}$  were included for several examples, excluding those with twisted misorientation angles due to skewed MSD values caused by NPs' rotational motions. While in NPs with tilted misorientation angles, atoms traversed straight paths from their initial positions to the neck region in bundles; in NPs with twisted misorientation angles, their direct path to the neck was disrupted by a tangential component as NPs were untwisting (e.g., compare [Figure 10A](#) and [Figure 10B](#)). Temporary GBs in NPs with twisted misorientations led to possibly less effective sintering relative to those with tilted misorientations. The defect analysis from Section "Analysis of defects to assess crystallographic defect-

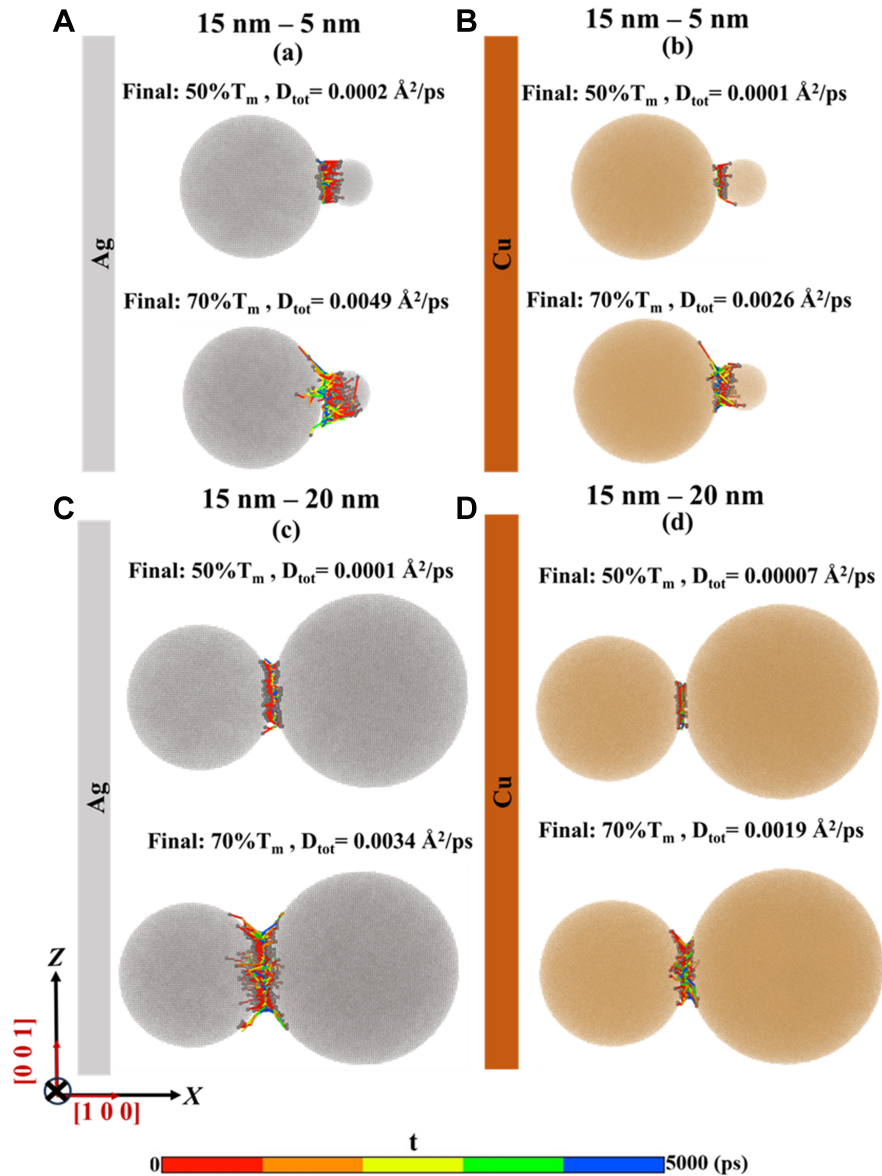


**Figure 9.** Examples of atomic trajectories of unequal-sized NPs sintered at 50% $T_m$  and 70% $T_m$ . Size ratios: (A) Ag, 3:1; (B) Cu, 3:1; (C) Ag, 1.33:1; (D) Cu, 1.33:1. See [Supplementary Materials](#) for animations of selected key events. NPs: Nanoparticles;  $T_m$ : bulk melting points.

mediated sintering mechanisms” suggests that the dislocations formed at the neck of the tilted NPs may have provided effective mass diffusion channels and facilitated the sintering. The dislocations on the tilt GB plane were edge dislocations which have given the tilt GBs thermal stability. Conversely, the screw dislocations at the neck of twisted NPs were mobile and could escape through the surface. The escape of the screw dislocations was accompanied by the untwisting of the particles and reduced the amount of effective mass diffusion channels, inhibiting effective atom transport. This behavior was consistent with the smaller neck size observed in sintered NPs with twisted misorientations, as reported in a previous study<sup>[12]</sup>. Hence, given the observed atomic trajectories, GB diffusion from tilted misorientations appeared more effective relative to diffusion from twisted misorientations. Moreover, the effectiveness of sintering mechanisms was higher for a 36° tilt misorientation than 53° tilt, as reflected in  $D_{tot}$  values (e.g., compare [Figure 10A](#) and

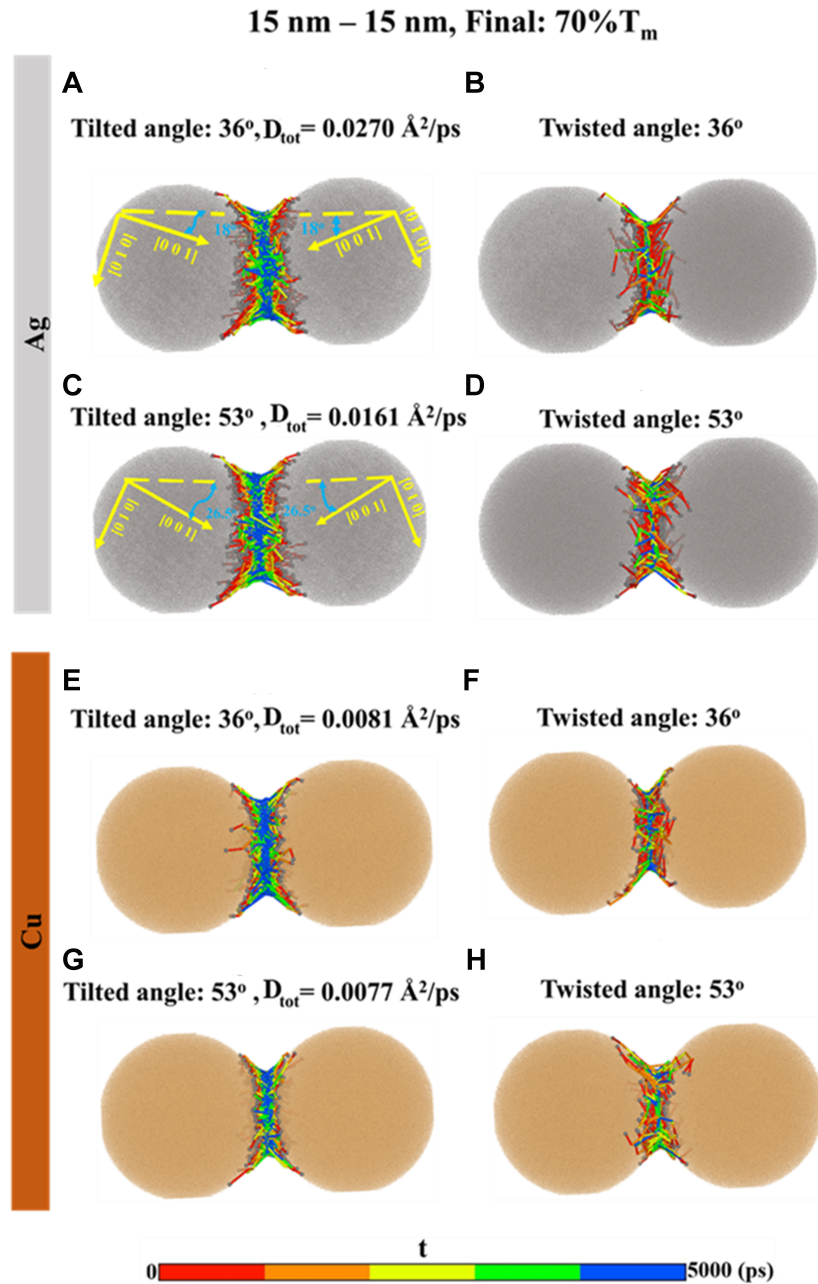


**Figure 10.** Examples of atomic trajectories of 15 nm diameter NPs with tilt and twist misorientation angles (36.87° and 53.15°) sintered at 70% $T_m$ : (A-D) Ag NPs and (E-H) Cu NPs. See [Supplementary Materials](#) for animations of selected key events. NPs: Nanoparticles;  $T_m$ : bulk melting points.

Figure 10C) and for Ag NPs than Cu ones (e.g., compare [Figure 10A](#) and [Figure 10E](#)).

As the diffusion mechanisms transition throughout the simulation, isolating and quantifying individual diffusion coefficients for lattice, surface, GB, and pipe diffusion was challenging. Instead, the  $D_{tot}$  was reported to reflect the resultant effect of all contributing mechanisms. Individual atoms were noticed to move along the surfaces of NPs toward the neck in all the studied NPs (i.e., equal/ unequal size, tilted/ twisted). This observation suggested that surface diffusion was a prevalent mechanism during sintering

regardless of NP size or orientation.

## PERSPECTIVE AND OUTLOOK

This study advanced the understanding of crystallographic defect-mediated and diffusion-based sintering mechanisms in NPs by addressing the previously overlooked episodic and condition-specific sintering mechanisms. These critical insights provide a foundation for more accurately developing data-driven and mechanism-oriented predictive models.

Building upon these findings, it is important to consider how these mechanisms apply to different materials, such as those with much higher melting points. For NPs made of hard-to-sinter alloys, such as W- and Mo-based ones<sup>[59,60]</sup>, higher sintering temperatures would be required. This is exemplified by the difference between Cu and Ag investigated in this study; the higher melting point of Cu compared to Ag necessitated higher sintering temperatures. Furthermore, when these refractory metals are alloyed with the ones with lower melting points, as in Cu-W, not only the mismatch in melting points but also the miscibility of the elements become critical factors influencing sintering behavior. Applying the model developed in this study to these hard-to-sinter metals and their alloys would require necessary adjustments in these regards.

Another aspect to consider is the possible effect of external factors, such as oxidation on the sintering process under specific conditions, such as prolonged exposure to elevated temperature and oxygen<sup>[61,62]</sup>. While oxidation could indeed play a role, its influence on this study is likely minimal due to the extremely brief NP sintering duration (~ns) and the argon-shielded environment in which NP sintering occurred. As a follow-on work, atomistic simulations of oxidation can be performed for more in-depth analysis, incorporating interatomic potentials between metal and oxygen<sup>[63]</sup>.

Expanding on the temperature-dependent aspects of sintering, it is worth noting that this study focused on solid-state sintering, which occurs below the melting points of both bulk and NPs due to significant reductions in NP melting temperatures caused by surface tension effects. Consequently, this study did not explore temperatures at or above the melting points of either bulk materials or NPs. However, a literature review suggests that higher temperatures can influence phonon behavior by increasing the presence of high-energy phonons and expanding phonon populations, which can (1) create defects by disrupting the regular atomic arrangements; (2) cause existing defects to disappear through the redistribution of atoms; or (3) cause defects to migrate through atomic redistribution<sup>[64,65]</sup>. As temperatures approach or exceed the melting point of NPs, certain defect populations such as dislocations and GBs tend to decrease. This occurs because the crystalline order breaks down, leading to a disordered liquid phase where such defects no longer exist in the same form. This is particularly relevant for Ag and Cu, which, unlike liquid crystals, lack short-range order in their liquid state<sup>[66,67]</sup>. Further research into phonon behavior in solid-state sintering and the transition to liquid-state sintering in NPs could provide valuable insights into defect evolution across different temperatures.

## CONCLUSION

This study delved into the intricate mechanisms governing sintering in equal- and unequal-sized NPs, and NPs with tilted and twisted misorientations. By utilizing MD simulations, the defects were visualized to elucidate the time dependence of lattice diffusion, GB diffusion, and a mechanism mediated by plastic deformation. Moreover, the existence of surface diffusion and the overall effectiveness of all the diffusion-based sintering mechanisms were investigated. The following conclusions were drawn:

1. The effectiveness of lattice diffusion mechanism in sintering was indicated by observing a higher concentration of vacancies at higher temperatures. For larger NPs, vacancies were noticed to remain mobile throughout the sintering process.
2. During sintering, diffusion of atoms facilitated plastic deformation through dislocation motions. However, interactions between dislocations themselves, and between dislocations and vacancies could impede their movements and influence their characteristics, such as length. These interactions which depended on the initial NP size, sintering temperature, and the material type, influenced the overall diffusion rate and the outcome of sintering, such as the final neck size.
3. NPs with tilted and twisted misorientations exhibited distinct GBs-facilitated diffusion behavior. NPs with tilted misorientations, characterized by edge dislocations in their GBs, displayed stable GBs throughout the simulation. In contrast, NPs with twisted misorientation angles possessed screw dislocations within their GBs. The repulsive forces between these screw dislocations caused a decrease in their density and ultimately led to untwisting of the NPs. This suggested that GB diffusion in NPs with twisted misorientations was active only during the initial stage of sintering, even though some residual dislocations might persist after GB disappearance.
4. Every simulated case revealed atomic diffusion paths confined to NP surfaces, implying the prevalence of surface diffusion as a governing mechanism. Higher temperatures, smaller NPs, and NPs with GBs all favored the overall effectiveness of the sintering mechanisms, as evidenced by numerous long-range trajectory lines and greater  $D_{tot}$ .

Understanding fundamental sintering mechanisms and their responses to different sintering conditions and NP characteristics allows for the design of new sintering feedstocks and optimization of sintering conditions, ultimately leading to enhanced sintering effectiveness.

## DECLARATIONS

### Authors' contributions

Conceptualization, methodology, investigation, validation, formal analysis, data curation, writing - original draft, visualization: Jamshideasli D

Conceptualization, methodology, investigation, resources, formal analysis, writing - review and editing, funding acquisition: Mahjouri-Samani M

Conceptualization, methodology, resources, investigation, formal analysis, writing - review and editing, supervision, project administration, funding acquisition: Shamsaei N

Conceptualization, methodology, investigation, resources, formal analysis, supervision, writing - review and editing: Shao S

### Availability of data and materials

The datasets generated and analyzed during the current study are available from the corresponding author upon reasonable request.

### Financial support and sponsorship

This work was supported by the U.S. National Science Foundation (NSF) under grant No. 2134024.

### Conflicts of interest

Shamsaei N and Shao S are Editorial Board Members of the *Green Manufacturing Open*, while the other authors have declared that they have no conflicts of interest.

### Ethical approval and consent to participate

Not applicable.

### Consent for publication

Not applicable.

### Copyright

© The Author(s) 2024.

## REFERENCES

1. Rasiya G, Shukla A, Saran K. Additive manufacturing - a review. *Mater Today* 2021;47:6896-901. DOI
2. Ahmadi Z, Lee S, Unocic RR, Shamsaei N, Mahjouri-Samani M. Additive nanomanufacturing of multifunctional materials and patterned structures: a novel laser-based dry printing process. *Adv Mater Technol* 2021;6:2001260. DOI
3. Ahmadi Z, Lee S, Patel A, Unocic RR, Shamsaei N, Mahjouri-Samani M. Dry printing and additive nanomanufacturing of flexible hybrid electronics and sensors. *Adv Mater Inter* 2022;9:2102569. DOI
4. Martins R, Gaspar D, Mendes MJ, et al. Papertronics: multigate paper transistor for multifunction applications. *Appl Mater Today* 2018;12:402-14. DOI
5. Singh R, Sharma V. Nano tungsten carbide interactions and mechanical behaviour during sintering: a molecular dynamics study. *Comput Mater Sci* 2021;197:110653. DOI
6. Bordia RK, Kang SL, Olevsky EA. Current understanding and future research directions at the onset of the next century of sintering science and technology. *J Am Ceram Soc* 2017;100:2314-52. DOI
7. Kockerbeck Z. Investigation of intensive pulsed light sintering for conductive hybrid copper ink. 2019. Available from: <https://prism.ualgary.ca/server/api/core/bitstreams/141c740d-fcec-4939-a1c9-43a6c7889387/content>. [Last accessed on 26 Sep 2024].
8. Yan F, Zhang X, Yang C, Hu B, Qian W, Song Z. Data-driven modelling methods in sintering process: current research status and perspectives. *Can J Chem Eng* 2023;101:4506-22. DOI
9. Pan J, Le H, Kucherenko S, Yeomans J. A model for the sintering of spherical particles of different sizes by solid state diffusion. *Acta Mater* 1998;46:4671-90. DOI
10. Buesser B, Gröhn AJ, Pratsinis SE. Sintering rate and mechanism of TiO<sub>2</sub> nanoparticles by molecular dynamics. *J Phys Chem C Nanomater Interfaces* 2011;115:11030-5. DOI PubMed PMC
11. Yang G, Lai H, Lin W, et al. A quantitative model to understand the microflow-controlled sintering mechanism of metal particles at nanometer to micron scale. *Nanotechnology* 2021;32:505721. DOI PubMed
12. Jamshideasli D, Mahjouri-samani M, Shamsaei N, Shao S. Molecular dynamics simulations of nanoparticle sintering in additive nanomanufacturing: the role of particle size, misorientation angle, material type, and temperature. *Mater Today Commun* 2024;39:108877. DOI
13. Zhu H. Sintering processes of two nanoparticles: a study by molecular dynamics simulations. *Phil Mag Lett* 1996;73:27-33. DOI
14. Yang Y, Li Z, Yang S, Li Y, Huang J. Multiscale simulation study of laser sintering of inkjet-printed silver nanoparticle inks. *Int J Heat Mass Tran* 2020;159:120110. DOI
15. Rahaman MN. 2 - Kinetics and mechanisms of densification. In: *Sintering of advanced materials*. Elsevier; 2010. pp. 33-64. DOI
16. Song P, Wen D. Molecular dynamics simulation of the sintering of metallic nanoparticles. *J Nanopart Res* 2010;12:823-9. DOI
17. Alshammery AOA. Modelling sintering at particle scale using variational and molecular dynamic methods. 2018. Available from: [https://figshare.le.ac.uk/articles/thesis/Modelling\\_sintering\\_at\\_particle\\_scale\\_using\\_variational\\_and\\_molecular\\_dynamic\\_methods/10199432?file=18381725](https://figshare.le.ac.uk/articles/thesis/Modelling_sintering_at_particle_scale_using_variational_and_molecular_dynamic_methods/10199432?file=18381725). [Last accessed on 26 Sep 2024]
18. German RM. Chapter three - Infrastructure developments. In: *Sintering: from empirical observations to scientific principles*. Elsevier; 2014. pp. 41-69. DOI
19. Zeng P, Zajac S, Clapp P, Rifkin J. Nanoparticle sintering simulations. *Mat Sci Eng A* 1998;252:301-6. DOI
20. Gu M, Liu T, Xiao X, Li G, Liao W. Simulation and experimental study of the multisized silver nanoparticles sintering process based on molecular dynamics. *Nanomaterials* 2022;12:1030. DOI PubMed PMC
21. Hu Y, Wang Y, Yao Y. Molecular dynamics on the sintering mechanism and mechanical feature of the silver nanoparticles at different temperatures. *Mater Today Commun* 2023;34:105292. DOI
22. Zhang L, Shibuta Y, Lu C, Huang X. Interaction between nano-voids and migrating grain boundary by molecular dynamics simulation. *Acta Mater* 2019;173:206-24. DOI
23. Lange A, Samanta A, Majidi H, et al. Dislocation mediated alignment during metal nanoparticle coalescence. *Acta Mater*

- 2016;120:364-78. DOI
24. Rojek J, Nosewicz S, Maździarz M, Kowalczyk P, Wawrzyk K, Lumelskyj D. Modeling of a sintering process at various scales. *Procedia Eng* 2017;177:263-70. DOI
  25. Alarifi H, Hu A, Yavuz M, Zhou YN. Silver nanoparticle paste for low-temperature bonding of copper. *J Electron Mater* 2011;40:1394-402. DOI
  26. Pan J. Solid-state diffusion under a large driving force and the sintering of nanosized particles. *Phil Mag Lett* 2004;84:303-10. DOI
  27. Pan H, Ko SH, Grigoropoulos CP. The solid-state neck growth mechanisms in low energy laser sintering of gold nanoparticles: a molecular dynamics simulation study. *J Heat Transfer* 2008;130:092404. DOI
  28. Sestito JM, Abdeljawad F, Harris TA, Wang Y, Roach A. An atomistic simulation study of nanoscale sintering: the role of grain boundary misorientation. *Comput Mater Sci* 2019;165:180-9. DOI
  29. Zeng P. Computer simulation of nanoparticle sintering. 1999. Available from: <https://digitalcommons.lib.uconn.edu/dissertations/AAI9926306>. [Last accessed on 26 Sep 2024]
  30. Callister WD Jr. Mitchell, Materials science and engineering: an introduction. 7th edition. John Wiley & Sons New York, 2007. Available from: <https://bcs.wiley.com/he-bcs/Books?action=index&itemId=0471736961&bcsId=2971>. [Last accessed on 26 Sep 2024].
  31. Mishin Y, Herzig C, Bernardini J, Gust W. Grain boundary diffusion: fundamentals to recent developments. *Int Mater Rev* 1997;42:155-78. DOI
  32. Sai Rajeshwari K, Sankaran S, Hari Kumar KC, et al. Grain boundary diffusion and grain boundary structures of a Ni-Cr-Fe- alloy: evidences for grain boundary phase transitions. *Acta Mater* 2020;195:501-18. DOI
  33. Legros M, Dehm G, Arzt E, Balk TJ. Observation of giant diffusivity along dislocation cores. *Science* 2008;319:1646-9. DOI PubMed
  34. Hirth JP, Lothe J. Theory of dislocations, 1992. [https://books.google.com/books/about/Theory\\_of\\_Dislocations.html?id=LFZGAAAYAAJ](https://books.google.com/books/about/Theory_of_Dislocations.html?id=LFZGAAAYAAJ). [Last accessed on 26 Sep 2024].
  35. Smith WF, Hashemi J. Crystal and amorphous structures in materials. In: Foundations of materials science and engineering. Available from: [http://sutlib2.sut.ac.th/sut\\_contents/H97858.pdf](http://sutlib2.sut.ac.th/sut_contents/H97858.pdf). [Last accessed on 26 Sep 2024].
  36. Pike NA, Løvvik OM. Calculation of the anisotropic coefficients of thermal expansion: a first-principles approach. *Comput Mater Sci* 2019;167:257-63. DOI
  37. Scola J, Tassart X, Vilar C, et al. Microstructure and electrical resistance evolution during sintering of a Ag nanoparticle paste. *J Phys D Appl Phys* 2015;48:145302. DOI
  38. Zhou XW, Johnson RA, Wadley HNG. Misfit-energy-increasing dislocations in vapor-deposited CoFe/NiFe multilayers. *Phys Rev B* 2004;69:144113. DOI
  39. Mendeleev M, King A. The interactions of self-interstitials with twin boundaries. *Philos Mag* 2013;93:1268-78. DOI
  40. Huang P, Hsu P, Huang T, Chou C. Laser sintering of Cu nanoparticles: analysis based on modified continuum-atomistic model. *Appl Phys A* 2020;126:3213. DOI
  41. Haslam A, Phillpot S, Wolf D, Moldovan D, Gleiter H. Mechanisms of grain growth in nanocrystalline fcc metals by molecular-dynamics simulation. *Mater Sci Eng A* 2001;318:293-312. DOI
  42. Nelli D, Cerbelaud M, Ferrando R, Minnai C. Tuning the coalescence degree in the growth of Pt-Pd nanoalloys. *Nanoscale Adv* 2021;3:836-46. DOI PubMed PMC
  43. Taba A, Ahmadi Z, Patel A, et al. Dry-printing conductive circuit traces on water-soluble papers. *ACS Sustain Chem Eng* 2023;11:16407-16. DOI
  44. Ghosh P, Lu J, Chen Z, Yang H, Qiu M, Li Q. Photothermal-induced nanowelding of metal–semiconductor heterojunction in integrated nanowire units. *Adv Elect Mater* 2018;4:1700614. DOI
  45. Sisáková K, Oriňak A, Oriňaková R, et al. Methane decomposition over modified carbon fibers as effective catalysts for hydrogen production. *Catal Lett* 2020;150:781-93. DOI
  46. Wei X, Zhang J, Xu K. The energy and structure of (0 0 1) twist grain boundary in noble metals. *Appl Surf Sci* 2006;253:854-8. DOI
  47. Ayadi A, Laib H, Khalfallah O. Relationship between structure and energy of symmetric tilt grain boundaries in Ag and Ni. *Acta Phys Pol A* 2020;138:528-32. DOI
  48. Thompson AP, Aktulga HM, Berger R, et al. LAMMPS - a flexible simulation tool for particle-based materials modeling at the atomic, meso, and continuum scales. *Comput Phys Commun* 2022;271:108171. DOI
  49. Stukowski A. Visualization and analysis of atomistic simulation data with OVITO—the open visualization tool. *Modelling Simul Mater Sci Eng* 2010;18:015012. DOI
  50. Sheppard D, Terrell R, Henkelman G. Optimization methods for finding minimum energy paths. *J Chem Phys* 2008;128:134106. DOI PubMed
  51. Larsen PM, Schmidt S, Schiøtz J. Robust structural identification via polyhedral template matching. *Modelling Simul Mater Sci Eng* 2016;24:055007. DOI
  52. Pozzi M, Jonak Dutta S, Kuntze M, et al. Visualization of the high surface-to-volume ratio of nanomaterials and its consequences. *J Chem Educ* 2024;101:3146-55. DOI PubMed PMC
  53. Kittel C. Introduction to solid state physics, 8th edition. John Wiley & Sons, Inc. Available from: <http://metal.elte.hu/~groma/Anyagtudomany/kittel.pdf>. [Last accessed on 26 Sep 2024].

54. Meyer R, Lewis LJ. Stacking-fault energies for Ag, Cu, and Ni from empirical tight-binding potentials. *Phys Rev B* 2002;66:052106. DOI
55. George Ellwood D. Mechanical metallurgy. Available from: [https://stu.westga.edu/~bthibau1/MEDT%207477-Cooper/Calibre%20Library/Dieter\\_%20George%20Ellwood/Mechanical%20metallurgy%20\(13\)/Mechanical%20metallurgy%20-%20Dieter\\_%20George%20Ellwood.pdf](https://stu.westga.edu/~bthibau1/MEDT%207477-Cooper/Calibre%20Library/Dieter_%20George%20Ellwood/Mechanical%20metallurgy%20(13)/Mechanical%20metallurgy%20-%20Dieter_%20George%20Ellwood.pdf). [Last accessed on 26 Sep 2024].
56. Hertzberg RW, Saunders H. Deformation and fracture mechanics of engineering materials (2nd Edition). *J Pressure Vessel Technol* 1985;107:309-11. DOI
57. Cormier VF, Bergman MI, Olson PL. Chapter 7 - Inner core dynamics. In: Earth's core. Elsevier; 2022. pp. 215-46. DOI
58. Alarifi HA, Atis M, Özdoğan C, Hu A, Yavuz M, Zhou Y. Molecular dynamics simulation of sintering and surface premelting of silver nanoparticles. *Mater Trans* 2013;54:884-9. DOI
59. Majumdar S, Raveendra S, Samajdar I, Bhargava P, Sharma I. Densification and grain growth during isothermal sintering of Mo and mechanically alloyed Mo-TZM. *Acta Mater* 2009;57:4158-68. DOI
60. Pan S, Yao G, Cui Y, et al. Additive manufacturing of tungsten, tungsten-based alloys, and tungsten matrix composites. *Tungsten* 2023;5:1-31. DOI
61. Lumley RN, Sercombe TB, Schaffer GM. Surface oxide and the role of magnesium during the sintering of aluminum. *Metall Mater Trans A* 1999;30:457-63. DOI
62. Schaffer GB, Hall BJ, Bonner SJ, Huo SH, Sercombe TB. The effect of the atmosphere and the role of pore filling on the sintering of aluminium. *Acta Mater* 2006;54:131-8. DOI
63. Hong S, van Duin AC. Molecular dynamics simulations of the oxidation of aluminum nanoparticles using the ReaxFF reactive force field. *J Phys Chem C* 2015;119:17876-86. DOI
64. Raj R, Kulkarni A, Lebrun J, Jha S. Flash sintering: a new frontier in defect physics and materials science. *MRS Bulletin* 2021;46:36-43. DOI
65. Bebek MB, Stanley CM, Gibbons TM, Estreicher SK. Temperature dependence of phonon-defect interactions: phonon scattering vs. phonon trapping. *Sci Rep* 2016;6:32150. DOI PubMed PMC
66. Zhang J, Wang X, Zhu Y, et al. Molecular dynamics simulation of the melting behavior of copper nanorod. *Comput Mater Sci* 2018;143:248-54. DOI
67. Alarifi HA, Atis M, Özdoğan C, Hu A, Yavuz M, Zhou Y. Determination of complete melting and surface premelting points of silver nanoparticles by molecular dynamics simulation. *J Phys Chem C* 2013;117:12289-98. DOI